PNAS RESEARCH ARTICLE | APPLIED PHYSICAL SCIENCES OPEN ACCESS

Ion transport control in electrolytes via electrochemical doping

Zhiwei Li[a], Yinghong Xu[a], Wanheng Lu[a], Xinglong Pan[a], Langyuan Wu[b], Wei Li Ong[a], Netanel Shpigel[b], Gang Chen[c,1], and Ghim Wei Ho[a,d,1]

Contributed by Gang Chen; received November 10, 2025; accepted January 11, 2026; reviewed by Chris Rhys Bowen and Liangbing Hu

Doping to control carrier (electron or hole) transport is foundational to modulate the properties of semiconductors, enabling the development of homojunctions and heterojunctions for integrated electronics. Unlike semiconductors with unipolar charge-carrier dominance, both cations and anions in electrolytes are mobile, which is undesirable for many applications. Here, we report a universal strategy to dope electrolytes such that the ion transport can be unipolar by incorporating electroactive polymers within hydrogels that interact discriminately with one type of ion via redox and binding mechanisms, leaving the counterions mobile. This transforms the system into an active, selective conductor that directs ion flow with high precision. We demonstrate the generality of this strategy using a wide range of electroactive polymers and ions. Particularly, we use emeraldine base and leucoemeraldine base, derived from polyaniline to create both n-type and p-type conductors with high ion selectivity. This electrolyte doping strategy has significant implications beyond the developed thermoelectrochemical devices with boosted performance, with potential applications in supercapacitors, batteries, and electrochemical sensors.

electrolyte doping | selective ion transport | hydrogel | ionic thermoelectric materials | low-grade heat harvesting

Significance

Doping is a foundational concept in solid-state semiconductors, enabling precise control over electron and hole transport. However, a comparable approach in liquid or gel-based electrolytes remains elusive, where both cations and anions typically move without discrimination. This work demonstrates a universal electrochemical doping method using electroactive additives to selectively control ionic species in such media, which is essential for the development of advanced energy conversion and storage systems.

In solid-state semiconductors, including light-emitting diodes, photovoltaics, thermoelectrics, and photo- and electrocatalysts, doping is achieved by immobile dopant atoms that create mobile electrons or holes (1–3). Similar doping strategies, however, do not exist for liquid/gel-state electrolytes which rely on the motion of ions, because both cations and anions can drift or diffuse randomly under electrical fields and concentration gradients. The ability to control transport predominantly by one type of ion (selective ion transport) is highly desirable for many applications, for example, to improve the charge transfer ratio of batteries, supercapacitors, and thermoelectrochemical systems (4–6). In this work, we establish a strategy to enable such control by immobilizing counterions via electrochemical doping in gel-based electrolytes. We validate the effectiveness of this strategy using a wide range of electroactive additives (EAs) to create both n-type and p-type ionic conductors, with the demonstration of low-grade thermal energy conversion into electricity serving as proof of concept.

Although certainly important for batteries, the need for n-type and p-type ionic conductors is well illustrated through ionic thermoelectric cells (iTECs) analogous to inorganic thermoelectric generators (TEG), both of which have been explored for direct conversion of heat into electricity (7–9). Conventional TEGs fabricated from n-type and p-type semiconductors through heavy doping with phosphorus (P) or boron (B) (Fig. 1*A*) typically exhibit low Seebeck coefficients of ~100 μV K^{-1} (10–13) and are therefore connected electrically in series and thermally in parallel to boost the voltage output. In contrast, iTECs can achieve thermopower (S_i) reaching millivolts per Kelvin (mV K^{-1}) through a combination of the thermogalvanic and thermodiffusion effects (14–16). The thermogalvanic contribution (S_{tg}) arising from the entropy difference of redox couples and the thermodiffusive contribution (S_{td}) originating from differences in mobility and Eastman entropy of transfer between cations and anions (15, 17, 18). The contributions from cations and anions to S_{td} cancel each other since they diffuse in the same direction while carrying opposite Eastman entropy of transfer. Although both n-type and p-type iTEC materials have been reported (17–34), existing materials lack systematic doping control, which makes it difficult to synchronize the signs of S_{td} and S_{tg}.

Our strategy is to use EAs to adsorb and immobilize either cations or anions in the electrolyte via electrochemical reactions, leaving the counterions mobile. The charge donating/accepting moieties in the conducting segment are electrochemically activated, forming electroactive sites that adsorb and immobilize oppositely charged ions in the electrolyte, leaving the counterions to control the ionic transport in the electrolyte. Fig. 1*B* illustrates this concept using emeraldine base (EB) or leucoemeraldine base (LB), derived from emeraldine salt form of polyaniline (ES-PANi), as representative electroactive additives, chosen for its high electroactivity readiness in electrochemical doping into n-type (reduced

Author affiliations: [a]Department of Electrical and Computer Engineering, National University of Singapore, Singapore 117583, Singapore; [b]Department of Chemical Sciences, Ariel University, Ariel 40700, Israel; [c]Department of Mechanical Engineering, Massachusetts Institute of Technology, Cambridge, MA 02139; and [d]Department of Material Science and Engineering, National University of Singapore, Singapore 117583, Singapore

Author contributions: Z.L., G.C., and G.W.H. designed research; Z.L., Y.X., and G.W.H. performed research; W.L., X.P., L.W., and G.W.H. contributed new reagents/analytic tools; Z.L., Y.X., W.L., X.P., L.W., W.L.O., N.S., G.C., and G.W.H. analyzed data; and Z.L., Y.X., W.L., X.P., L.W., W.L.O., N.S., G.C., and G.W.H. wrote the paper.

Reviewers: C.R.B., University of Bath; and L.H., Yale University.

The authors declare no competing interest.

[1]To whom correspondence may be addressed. Email: gchen2@mit.edu or elehgw@nus.edu.sg.

This article contains supporting information online at https://www.pnas.org/lookup/suppl/doi:10.1073/pnas.2532302123/-/DCSupplemental.

Published February 11, 2026.

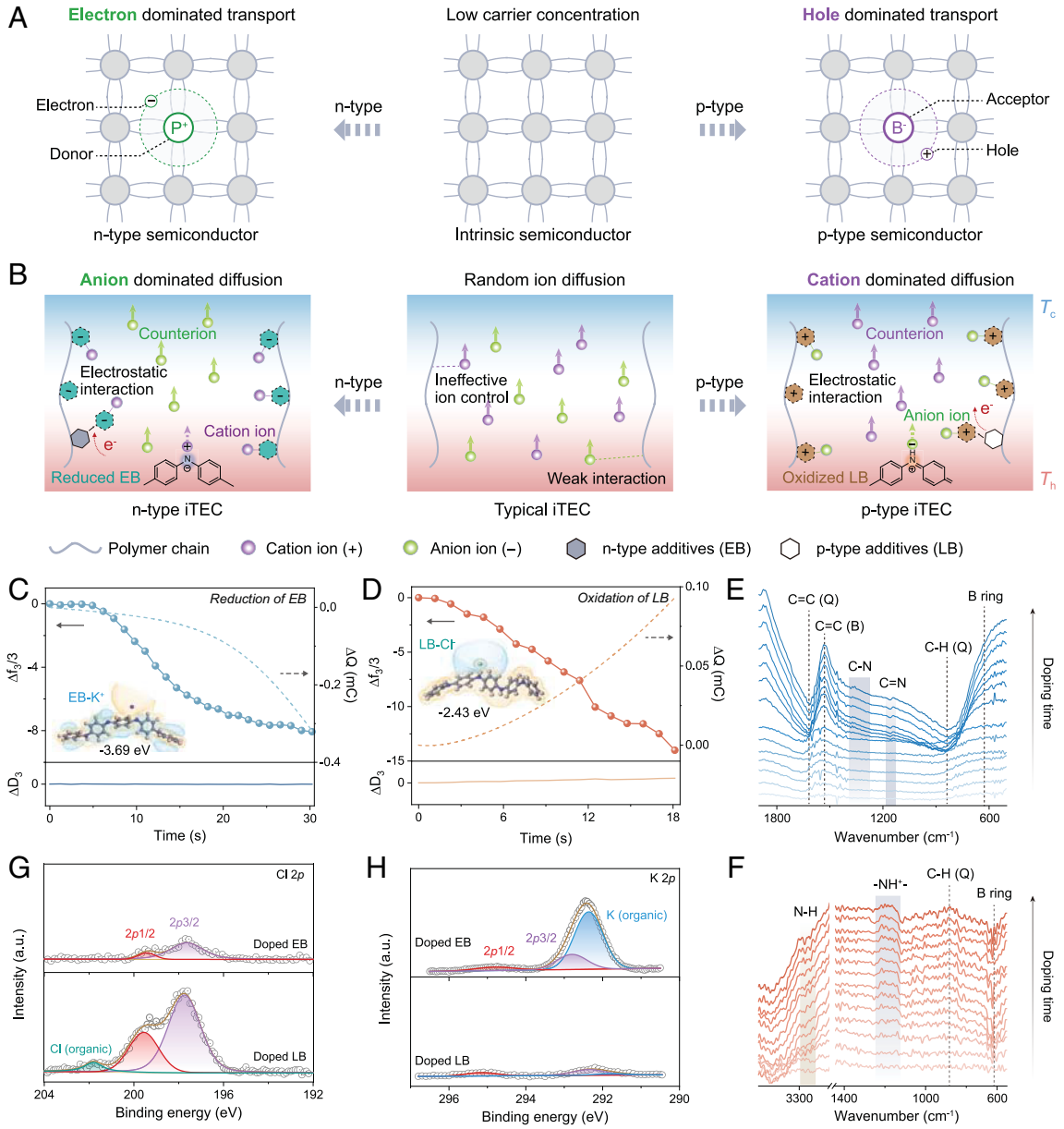

Fig. 1. Electrolyte doping enabled by electrochemical behavior of EA. (*A*) Carrier transport control by element doping in semiconductors. (*B*) Ion-selective diffusion in iTEC engineered by EA for p-type and n-type systems by electrochemical doping, respectively. EQCM-D analyses with 0.8 mol L^{-1} KCl electrolyte for (*C*) n-type doping (reduction) of EB, and (*D*) p-type doping (oxidation) of LB (Corresponding insets are calculated binding energies of LB-Cl^- and EB-K^+). In situ FTIR spectra during various electrochemical doping states of (*E*) EB and (*F*) LB, respectively. XPS spectrum of (*G*) Cl 2*p* and (*H*) K 2*p* for EB and LB after doping.

state) and p-type (oxidized state), respectively. This situation is fundamentally different from the physical element doping in inorganic semiconductors (Fig. 1*A*). For example, the P^+ sites are positively charged because they donate free electrons to the conduction band, while the B^- sites are negatively charged because they trap electrons, creating mobile holes. The doping of EA in electrolyte highly depends on its electrochemical reaction along with charge transfer. In EB, the -C=N- groups could be negatively charged to -C—N^-- by n-type electrochemical reduction enabling the adsorption of cations (35), leaving anions as the mobile conducting species, i.e., an anionic conducting electrolyte. Conversely, in LB, the -NH- moieties could be positively charged to -NH^+- by p-type electrochemical oxidation (36), facilitating the adsorption of anions, leaving cations as the ionic conducting species, i.e., a cation conducting electrolyte. Below, we will demonstrate effectiveness and universality of this doping strategy for controlling ionic conduction type, which opens a pathway for the rational design of high-performance ionic materials for diverse applications.

Results

Electrochemical Doping of EAs. The voltage of iTEC induced by ion diffusion under a temperature gradient is positively correlated with the concentration difference (ΔC) between cations and anions from the hot side to the cold side (12). In a typical iTEC without ion transport control (Fig. 1*B*), both cations and anions diffuse indiscriminately following the same temperature gradient, leading to a limited ΔC. Different from selective ion diffusion achieved by the weak interactions between ions and polymer chains (5), the introduction of EA is an effective and precise strategy to achieve a high ΔC as well as ΔV by reversibly immobilizing one type of ions through electrochemical reactions.

As a proof of concept, EB and LB are prepared and modified from ES-PANi by chemical treatments (described in the *Materials and Methods* section) as typical additives for n-type and p-type doping, respectively. X-ray diffraction (XRD) patterns and Fourier transform infrared spectroscopy (FTIR) spectra ascertain the successful preparation of EAs (*SI Appendix,* Figs. S1 and S2*A*). The N 1*s* spectra fitted from X-ray photoelectron spectroscopy (XPS) indicate the formation of dominated -NH- (66.5%) and -C═N- (67.2%) moieties in LB and EB (*SI Appendix,* Fig. S2*B*), respectively (35). Similar to the morphology of ES-PANi, both LB and EB show irregular particles of hundreds of nanometers (*SI Appendix,* Fig. S3 *A–C*), providing abundant active sites for doping. Electrochemical quartz crystal microbalance with dissipation monitoring (EQCM-D) was employed to investigate the ion-selective adsorption behavior of EB and LB in 0.8 mol L^{-1} KCl electrolyte (*SI Appendix*, Fig. S4 and Note S1) (37, 38). Fig. 1 *C* and *D* profile the time-dependent variations in normalized frequency ($\Delta f_3/3$), dissipation (ΔD_3), and accumulated charge (ΔQ). During the cathodic scan at negative potential range, the $\Delta f_3/3$ value of EB decreases with the negative charge accumulation, which suggests the cation (K^+) adsorption in EB (39). In contrast, LB exhibits the opposite behavior. When adopting the anodic scan at positive potential range to the LB, $\Delta f_3/3$ shifts downward along with the positive charge accumulation, indicating anion (Cl^-) adsorption in LB (39, 40). Meanwhile, the lower binding energies of EB-K^+ (–3.69 eV) and LB-Cl^- (–2.43 eV) compared to other clusters (i.e., AA-K^+/Cl^- and HEMA-K^+/Cl^-) further support the selective counter ion transport capability of EAs (*Insets* of Fig. 1 *C* and *D* and *SI Appendix,* Fig. S5). These distinct ion-adsorption behaviors can be attributed to their electrochemical reactions between the functional groups and ions, as revealed by *in-situ* FTIR measurements in Fig. 1 *E* and *F*. For EB with its half-oxidation state, the -C═N- (1,160 cm^{-1}) groups can be reduced to -C-N^-- (1,310 to 1,380 cm^{-1}) and react with cations like K^+ through n-type electrochemical reactions (Fig. 1*E*) (41). Notably, the obvious decrease of characteristic bands of quinonoid (Q) ring (1,611 cm^{-1} for C═C and 827 cm^{-1} for C-H) and increase of characteristic bands of benzenoid (B) ring (1,534 cm^{-1} for C═C and 650 cm^{-1} for B ring) further explain a structural transition from Q to B during n-type doping (*SI Appendix,* Fig. S6*A*) (41, 42). Conversely, owing to the high reduction state of LB, the -NH- (3,250 cm^{-1}) group undergoes single-electron p-type reaction and is oxidized to -NH^+- (1,130 to 1,210 cm^{-1}), attracting anions such as Cl^- (Fig. 1*F*) (35, 41). The increase of C-H (Q) at 860 cm^{-1} and decrease of B ring at 670 cm^{-1} suggests a structural evolution from B to Q during p-type doping (*SI Appendix,* Fig. S6*B*) (41). Besides, the normalized high-resolution X-ray photoelectron spectroscopy (XPS) Cl 2*p* and K 2*p* spectra of EB and LB after electrochemical process are employed to analyze the selective ion doping. Two typical peaks at 197.8 eV (Cl 2*p*3/2) and 199.3 eV (Cl 2*p*1/2) correspond to adsorbed Cl^- on the electrode surface (Fig. 1*G*) (42). The other two peaks in K 2*p* spectrum at 292.8 eV and 295.1 eV can be attributed to K 2*p*3/2 and K 2*p*1/2 of the adsorbed K^+ (Fig. 1*H*), respectively (43). Notably, the additional peak at 201.8 eV in Cl 2*p* spectra of doped LB and 292.3 eV in K 2*p* spectra of doped EB can be assigned to the bonded species by organic functional groups (42, 44). The distinctly high intensities of Cl^- in doped LB and K^+ in doped EB highlight the effectiveness of EAs in realizing selective ion transport through electrochemical doping.

Selective Ion Transport Tailored by Electrolyte Doping. To explore the ion diffusion behavior in electrolyte, the EA particles were mixed with 2-hydroxyethyl methacrylate (HEMA), acrylic acid (AA), and KCl solution, followed by gelation to form an inter-cross-linked hydrogel (labeled as PHA@x, where x denotes the type of EA) (*SI Appendix,* Fig. S3 *D–F*). The capability of EAs for dynamic ion control is systematically investigated using PHA@x hydrogels. Temperature-variable FTIR together with a two-dimensional correlation spectroscopy (2DCOS), based on the Noda's rule, was employed to study the thermosensitivity and reaction sequences of functional groups in n-type PHA@EB-KCl and p-type PHA@LB-KCl (45). The reaction sequence determined was -C═N- (~1,590 cm^{-1}) → -NH- (~3,230 cm^{-1}) → -COO^- (~1,637 cm^{-1}) → -COOH (~1,706 cm^{-1}) → -C═C- (~1,482 cm^{-1}), which indicates that the ions preferentially interact with electroactive groups from EB/LB (-C═N- and -NH-) rather than those from PHA chains (-COO^-, -COOH, -C═C-) (Fig. 2*A* and *SI Appendix*, Figs. S7 and S8 and Tables S1 and S2). Consistent with the simulated LUMO-HOMO energy levels (*Insets* in Fig. 3*A* and *SI Appendix,* Fig. S9), -C═N- functionalized EB tends to accept electrons, while LB including -NH- tends to donate electrons (36). To maintain charge neutrality, the -C—N^-- groups reduced from -C═N- in EB can be doped/coordinated by K^+, enabling Cl^- dominated diffusion under a temperature gradient, i.e., an n-type electrolyte. Similarly, LB releases electrons along with the doping/coordination of Cl^- through the oxidized -NH^+- from -NH- functional groups, resulting in K^+ dominated diffusion, i.e., a p-type electrolyte. The surface potential of PHA@EB-KCl exhibits a negative shift (from 0 to –15 mV) under a ΔT of ~3 K, while a positive shift (from 0 to 24 mV) is observed for PHA@LB-KCl (Fig. 2*B*), highlighting effective regulation of ion transport in electrolyte from random to selective.

The ion transport control behaviors of EAs in electrolytes were further verified by cyclic voltammetry (CV) tests. As shown in Fig. 2 *C* and *D*, the CV curve of PHA-KCl exhibits an almost rectangular shape, indicating its typical electrical double-layer capacitive behavior (46). However, the adsorption and desorption of K^+ below the potential of zero charge (PZC) are greatly limited owing to the lack of free K^+ in PHA@EB-KCl electrolyte (Fig. 2*C*). The slightly deformed adsorption/desorption process for Cl^- over PZC suggests ion diffusion is dominated by anions in the PHA@EB-KCl electrolyte, indicating n-type behavior. While for PHA@LB-KCl, the adsorption and desorption of Cl^- decrease due to the electrostatic interactions between Cl^- and LB (Fig. 2*D*). The well-maintained adsorption/desorption of K^+ in PHA@LB-KCl confirms its cation dominated diffusion, consistent with p-type characteristics. XPS mapping of K 2*p* and Cl 2*p* further supports these findings. EB displays relatively higher K^+ intensity than LB (Fig. 2*E*), implying effective immobilization of K^+ by EB. While the intensity of Cl^- in LB is much higher than EB (Fig. 2*F*), confirming the immobilization of Cl^- by LB. In *SI Appendix,* Fig. S10, we show the open-circuit voltage (V_{oc}) developed across PHA@EB-KCl and PHA@LB-KCl electrolytes as a function of applied temperature difference (ΔT). The slope fitted in Fig. 2*G* shows that the S_i for PHA@EB-KCl reached –6.4 ± 0.2 mV K^{-1}, consistent with its n-type characteristics, while PHA@LB-KCl is p-type, with a S_i value of 2.0 ± 0.1 mV K^{-1}.

Electrolyte Doping–Boosted iTEC Performances. Thermodiffusion effect can be combined with thermogalvanic effect to boost the performance of iTECs (12), as shown in Fig. 3*A*, where KCl and $K_4[Fe(CN)_6]/K_3[Fe(CN)_6]$ ($FeCN^{4-/3-}$) or $FeCl_2/FeCl_3$ ($Fe^{3+/2+}$) serve as the thermodiffusion and thermogalvanic species, respectively. The ability to dope electrolytes enables us to synergize the two effects. We demonstrate this ability using PC@G as electrodes together with hydrogel electrolytes. The PC@G electrode, composed of carbon microparticles, provides a large surface area for ion adsorption/desorption and continuous pathways for charge transfer (*SI Appendix,* Fig. S11). Under a temperature gradient, PHA-KCl, PHA-$Fe^{3+/2+}$, and PHA-$FeCN^{4-/3-}$ exhibit n-type thermodiffusion, n-type thermogalvanic, and p-type thermogalvanic behavior (Fig. 3*B*),

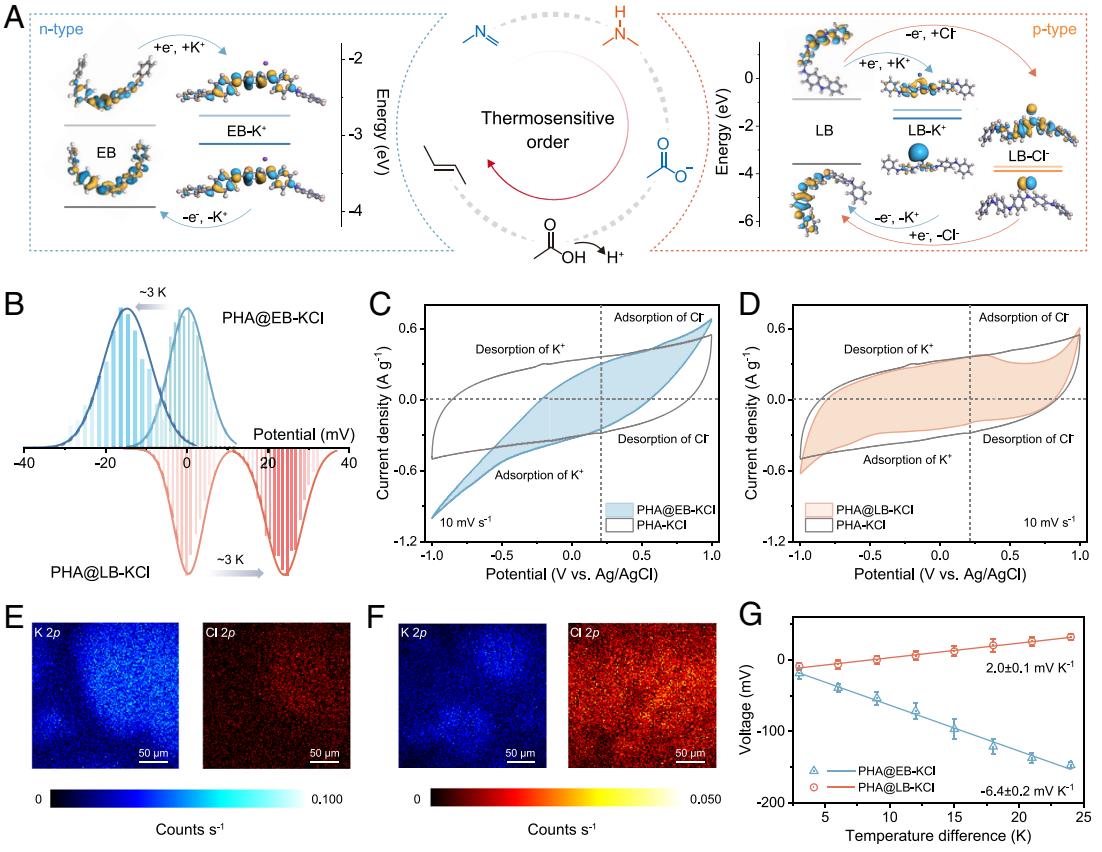

Fig. 2. Dynamical ion and electron transport control by EA. (*A*) Schematic diagram of thermosensitive groups sequence for boosted ion selectivity, together with the possible electrochemical processes (the blue region represents the n-type reactions between EA and K^+; the red region is the p-type reactions between EA and Cl^-. *Insets* summarize the corresponding LUMO and HOMO level of EB, EB-K^+, LB, LB-K^+, and LB-Cl^-, respectively). (*B*) Evolution of surface potential for PHA@EB-KCl and PHA@LB-KCl with a ΔT of ~3 K (The hot side controlled by the heat stage is located below the gel, and the platinum tip at the cold side is used as working electrode). Comparison of CV curves at 10 mV s^{-1} for (*C*) PHA-KCl and PHA@EB-KCl and (*D*) PHA-KCl and PHA@LB-KCl. XPS mapping images of K 2*p* and Cl 2*p* for (*E*) EB and (*F*) LB after electrochemical doping, respectively. (*G*) Thermopower of PHA@EB-KCl and PHA@LB-KCl hydrogels. Error bars are the SD of voltage recorded.

respectively. If one combines PHA-KCl with PHA-$FeCN^{4-/3-}$, i.e., the PHA-KCl-$FeCN^{4-/3-}$, without doping control, the V_{oc} increases to 12.6 mV as ΔT rises from 3 to 12 K but declines at higher ΔT (12 to 24 K) due to competing thermodiffusion and thermogalvanic contributions (Fig. 3 *B* and *C*). In contrast, doping with LB (PHA@LB-KCl-$FeCN^{4-/3-}$) which immobilizes anions, results in a continuous increase in V_{oc} to 87.4 mV as a function of ΔT. Meanwhile, the n-type V_{oc} improves from −96 mV (PHA-KCl) to −237 mV (PHA-KCl-$Fe^{3+/2+}$) owing to the synergistic effect between thermodiffusion and thermogalvanic. By immobilizing cations with EB in PHA@EB-KCl-$Fe^{3+/2+}$, the V_{oc} further increases to −335 mV, which is ~141% higher than PHA-KCl-$Fe^{3+/2+}$. Mass tuning of LB (x = 0 to 1.2 mg) and EB (y = 0 to 0.8 mg) further optimizes the S_i from 0.47 ± 0.1 mV K^{-1} to 3.7 ± 0.04 mV K^{-1} for p-type iTECs (*SI Appendix,* Figs. S12 and S13) and from −10.1 ± 0.3 mV K^{-1} to −15.2 ± 0.6 mV K^{-1} for n-type iTECs (*SI Appendix,* Figs. S12 and S14), respectively. For simplicity, these optimized formulations are hereafter referred to as PHA@LB-KCl-$FeCN^{4-/3-}$ and PHA@EB-KCl-$Fe^{3+/2+}$, unless otherwise stated.

In-situ Raman spectroscopy was conducted to monitor real-time insights into the changes in $Fe^{3+/2+}$ and $FeCN^{4-/3-}$ concentrations under a temperature gradient. For PHA@LB-KCl-$FeCN^{4-/3-}$, the peak intensities of $FeCN^{4-}$ decrease, while those of $FeCN^{3-}$ increase with ΔT from 0 K to 18 K at the hot side (Fig. 3*D* and *SI Appendix,* Fig. S15*A*). Meanwhile, the peak intensities of $FeCN^{4-}$ increase and those of $FeCN^{3-}$ decrease at the cold side. Notable shifts in peak intensities of $FeCN^{4-}$ and $FeCN^{3-}$ observed at different temperature ranges indicate effectively limited thermodiffusion of $FeCN^{4-/3-}$ and dynamically facilitated redox behavior by the LB engineered hydrogel. However, the peak intensities of $FeCN^{4-}$ and $FeCN^{3-}$ in PHA-KCl-$FeCN^{4-/3-}$ without LB remain almost unchanged (*SI Appendix,* Figs. S15*B* and S16*A*). Compared to the ratio changes observed by in situ ultraviolet-visible (UV-vis) spectroscopy (*SI Appendix,* Figs. S18–S21, Tables S3 and S4, and Note S2) in PHA-KCl-$FeCN^{4-/3-}$ (*SI Appendix,* Fig. S22*A*), the LB-induced redox reactions in p-type PHA@LB-KCl-$FeCN^{4-/3-}$ led to a decreased $C_{Fe(CN)_6^{4-}}/C_{Fe(CN)_6^{3-}}$ ratio from 1.06 ± 0.02 to 0.90 ± 0.01 at the hot side and an increased ratio from 1.09 ± 0.03 to 1.37 ± 0.01 at the cold side, resulting in an extended ΔC (Fig. 3*F*). Similar phenomenon also can be found in n-type PHA-KCl-$Fe^{3+/2+}$ (*SI Appendix,* Figs. S16*B* and S17*A*), the Raman peak intensity of Fe^{2+} gradually increases while that of Fe^{3+} decreases at the hot side in PHA@EB-KCl-$Fe^{3+/2+}$, and the peak intensity of Fe^{2+} gradually decreases as that of Fe^{3+} increases at the cold side (Fig. 3*E* and *SI Appendix,* Fig. S17*B*). This leads to a decrease in the $C_{Fe^{3+}}/C_{Fe^{2+}}$ ratio from 1.04 ± 0.02 to 0.81 ± 0.01 and an increased ratio from 0.87 ± 0.02 to 1.06 ± 0.01 can be formed at the hot side and cold side of PHA@EB-KCl-$Fe^{3+/2+}$ (Fig. 3*G*). In comparison, PHA-KCl-$Fe^{3+/2+}$ without EB shows insignificant changes in the $C_{Fe^{3+}}/C_{Fe^{2+}}$ ratio in (*SI Appendix,* Fig. S22*B*). According to above analyses, electrochemical doping via electrolyte engineering can not only extend the concentration gradients by selectively tuning ion diffusion but also accelerate the confined redox reactions by transferring external electrons, offering a promising strategy for enhancing power/electricity generation capabilities of iTECs.

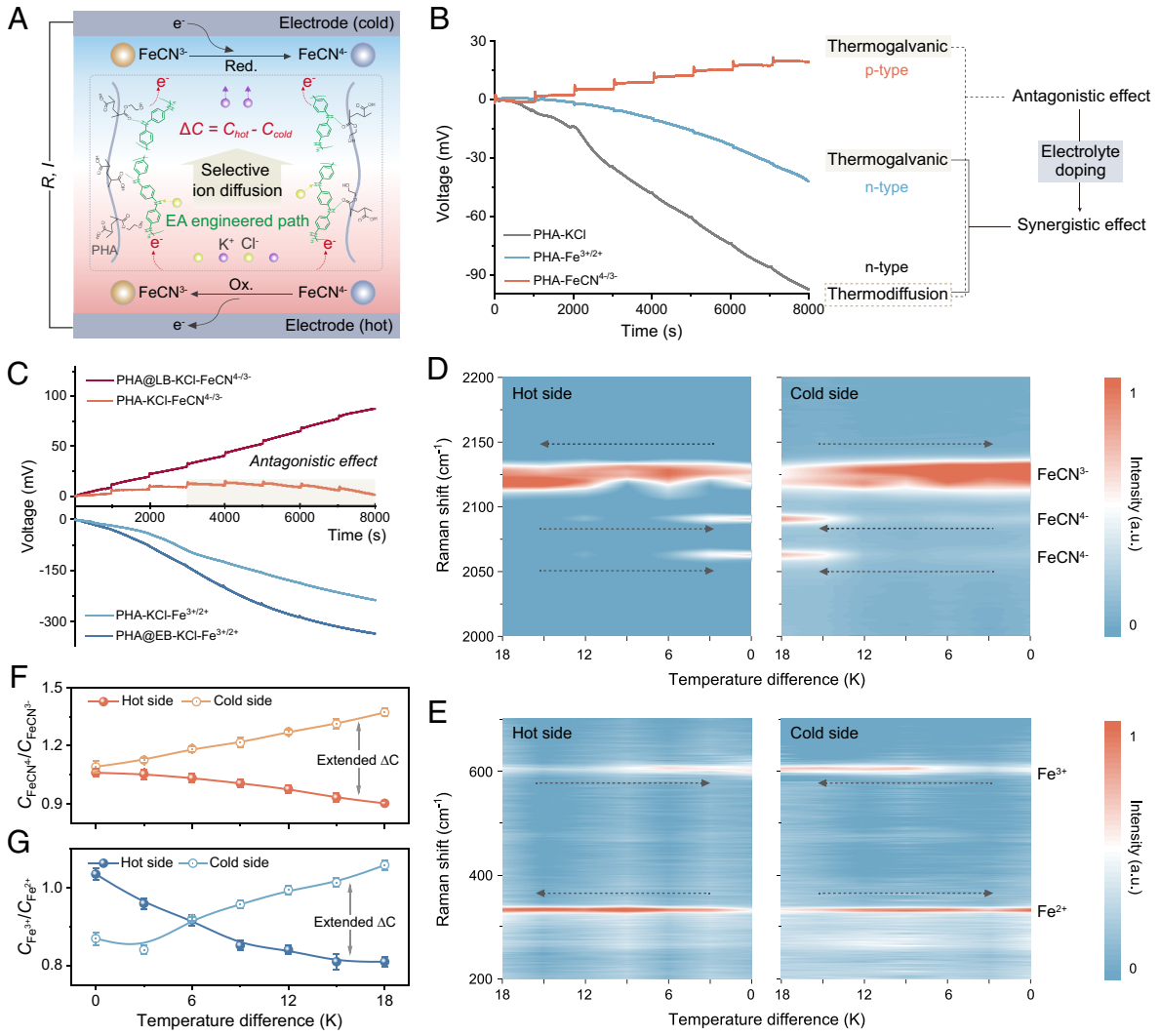

Fig. 3. Role of electrolyte doping on boosting iTEC performances. (*A*) Schematic illustration of selective ion diffusion enhanced p-type TEC based on the synergistic effect between thermodiffusion and thermogalvanic behaviors. (*B*) Thermal charging curves of PHA-based iTECs with KCl, $Fe^{3+/2+}$, and $FeCN^{4-/3-}$, respectively. (*C*) Voltage evolution of as-prepared hydrogels with/without EA at various temperature differences from 3 K to 24 K. In situ Raman spectra recorded from the hot and cold sides at various temperature differences for (*D*) PHA@LB-KCl-$FeCN^{4-/3-}$, and (*E*) PHA@EB-KCl-$Fe^{3+/2+}$. Concentration ratio changes of (*F*) $FeCN^{4-}/FeCN^{3-}$ and (*G*) Fe^{3+}/Fe^{2+} on the hot and cold sides obtained from the absorbance change in in situ UV-vis spectra (Error bars represent the SD of three repeated measurements).

Scalable Construction of Flexible n-/p-Units Integrated Modules. Due to significantly modified redox reactions kinetics by doped EAs (*SI Appendix,* Fig. S23), the iTEC units with EAs possess high voltage retention of 96.5% (PHA@EB-KCl-$Fe^{3+/2+}$) and 88.7% (PHA@LB-KCl-$FeCN^{4-/3-}$) over 50 thermal charge/electrical discharge cycles (*SI Appendix,* Fig. S24), further demonstrating the repeatability and durability of EA-engineered iTECs for practical heat-to-electricity conversion. The maximum power density (P_{max}) and normalized power density ($P_{max}/\Delta T^2$) of 1.43 W m^{-2}, 2.48 mW m^{-2} K^{-2} and 0.46 W m^{-2}, 0.80 mW m^{-2} K^{-2} can be achieved by respective PHA@EB-KCl-$Fe^{3+/2+}$ and PHA@LB-KCl-$FeCN^{4-/3-}$ (*SI Appendix,* Fig. S25*A*), whereas iTECs without EAs exhibit much lower values: 0.49 W m^{-2}, 0.85 mW m^{-2} K^{-2} for PHA-KCl-$Fe^{3+/2+}$ and 0.01 W m^{-2}, 0.02 mW m^{-2} K^{-2} for PHA-KCl-$FeCN^{4-/3-}$ (*SI Appendix,* Fig. S25*B*). Compared with previously reported n-/p-type iTECs (*SI Appendix,* Fig. S26 and Table S5) (12, 15, 21, 23–25, 28, 33, 34, 47–49), the as-developed PHA@EB-KCl-$Fe^{3+/2+}$ demonstrates a record-level competitiveness due to its superior absolute V_{oc} (335 mV), absolute S_i (15.2 mV K^{-1}), and $P_{max}/\Delta T^2$ (2.48 mW m^{-2} K^{-2}). Besides, the energy output and average power density (P_{ave}) for 2 h at ΔT of 24 K of n-type PHA@EB-KCl-$Fe^{3+/2+}$ and p-type PHA@LB-KCl-$FeCN^{4-/3-}$ iTECs are calculated as 264.1 mJ, 0.92 W m^{-2} and 89.4 mJ, 0.31 W m^{-2}, respectively (*SI Appendix,* Fig. S27). We also estimated thermal conductivities as 0.508 (PHA), 0. 582 (PHA@EB), and 0.627 W m^{-1} K^{-1} (PHA@LB) (*SI Appendix,* Fig. S28 and Note S3), comparable to water value of 0.615 W m^{-1} K^{-1}, and lower than typical thermoelectric materials such as ~1.5 W m^{-1} K^{-1} for Bi_2Te_3-alloys.

Previous iTEC device demonstrations were constructed using single-type units (either n-type or p-type), connected electrically in series and thermally in parallel with metallic electrodes running between the hot and cold sides to boost the voltage output, due to the lack of readily available matching pairs. The availability of both n-type and p-type iTEC materials in this work enables the scalable construction of integrated modules (Fig. 4*A*) (detailed in the Methods section). In addition, EA-contained hydrogels become mechanically tougher while remaining soft and stretchable compared to the pristine PHA (*SI Appendix,* Fig. S29), facilitating stable and conformal contact with rough electrode surfaces and resulting in slight resistance change even after mechanical deformation (*SI Appendix,* Fig. S30 and Note S4), which is beneficial for maintaining structural integrity for practical applications.

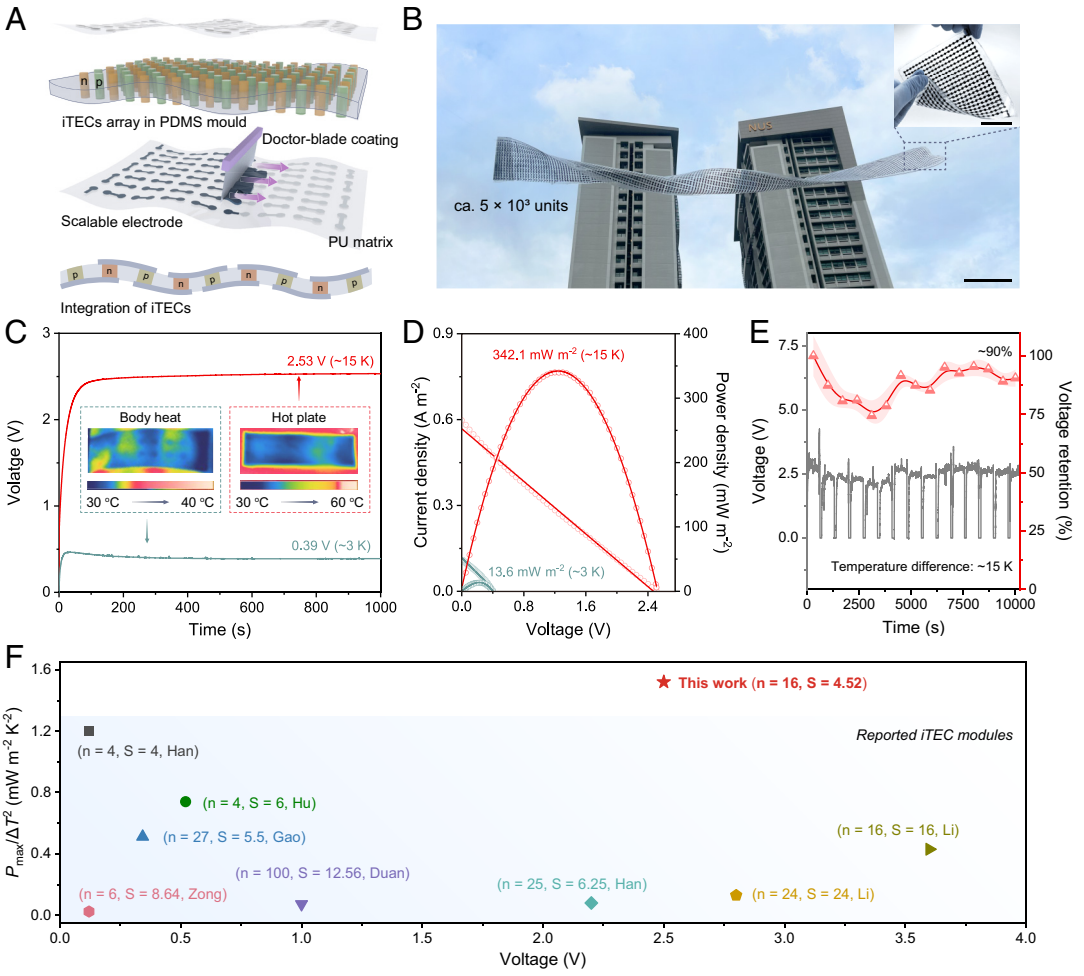

Fig. 4. Construction and electricity generation of integrated devices. (*A*) Schematic illustration of the device components and the heat-to-electricity conversion process of integrated n-p units (n and p units are PHA@EB-KCl-$Fe^{3+/2+}$ and PHA@LB-KCl-$FeCN^{4-/3-}$). (*B*) Digital image of a scalable and flexible device containing ca. 5 × 10^3 units. (Scale bar, 10 cm.) (The *Inset* shows as-assembled device with 400 units connected in series. (Scale bar, 5 cm.) (*C*) Real-time voltage curves for eight pairs of n-p units (effective area: 3.4 cm^{-2}) for harvesting small/large temperature difference (~3 K/~15 K) formed between body heat/hot plate and ambient. (*D*) Current density-voltage curves and corresponding power densities of n-p integrated device under various temperature differences. (*E*) Quasi-continuous open circuit voltage response and voltage retention versus time curves for 15 cycles (condition: thermal charge for 600 s, short circuit for 100 s, temperature difference: ~15 K). (*F*) Comparison of the power and voltage for recently reported iTEC modules (n represents the number of units, S (cm^2) represents the area of iTECs).

Fig. 4*B* shows a large-scale module measuring 150 cm × 12 cm (length × width) containing approximately 5 × 10^3 n-/p-type units with Π-type series connection. Electrochemical impedance spectroscopy (EIS) analysis of modules comprising eight pairs of n-p units suggests that the integration strategy is scalable and does not introduce appreciable resistive losses at the gel/electrode interfaces (*SI Appendix,* Fig. S31). When using eight pairs of n-p units as a demonstration, a high V_{oc} of ~2.5 V and a short-circuit current density of ~0.6 A m^{-2} can be achieved under a ΔT of ~15 K (Fig. 4*C*), delivering a corresponding P_{max} and P_{ave} of 342.1 mW m^{-2} and 297 mW m^{-2} (Fig. 4*D* and *SI Appendix,* Fig. S32). Even at different bending states, the module exhibits negligible variation with increasing bending angle, and retains ~91% of its initial value after bending at 135° (*SI Appendix,* Fig. S33). Moreover, under a small ΔT of ~3 K, generated between body heat and ambient conditions, the as-developed module achieved a V_{oc} of ~0.4 V and a P_{max} of 13.6 mW m^{-2}, demonstrating its attractive capability of harvesting low-grade heat near room temperature. Despite minor short-term fluctuations, the module maintained a consistent V_{oc} of 2.5 V and high voltage retention of ~90% after 15 cycles of thermal charging and discharging (Fig. 4*E*). This underlines good electromechanical durability and reliability of the flexible iTEC module for practical operation. The $P_{max}/\Delta T^2$ value of 1.52 mW m^{-2} K^{-2} for the integrated module also outperforms previously reported iTEC modules (Fig. 4*F* and *SI Appendix,* Table S6) (12, 24, 25, 47, 48, 50–52).

Generality of the Electrolyte Doping Strategy. To demonstrate the generality of the doping strategy, we have tested other electroactive polymers using 0.8 mol L^{-1} KCl electrolyte. Fig. 5*A* shows results of changing to different types of EA candidates, where n-type iTECs with negative S_i were achieved using EB, polydopamine (PDA), and perylenetetracarboxylic dianhydride (PTCDA) by immobilizing cations (*SI Appendix,* Figs. S10*A* and S34), while p-type iTECs with positive S_i were realized using LB, poly(3,4-ethylenedioxythiophene) (PEDOT) and polypyrrole (PPy) by immobilizing anions (*SI Appendix,* Figs. S10*B* and S35).

We also tested different types of ions (cation: Li^+, Na^+, K^+, NH_4^+, Zn^{2+}; anion: Cl^-, F^-, NO_3^-, SO_4^{2-}) using PHA@LB-*m* and PHA@EB-*m*. Consistent with Hofmeister series (53), SO_4^{2-}-based salts significantly disrupted gel formation due to their strong salting-out effect compared to other hydrogels (*SI Appendix,* Figs. S36 and S37 and Note S5). Upon introducing redox species, PHA@LB-*m*-$FeCN^{4-/3-}$ consistently exhibited p-type behavior with voltage output range from 40 mV to 119 mV (Fig. 5*B*), while PHA@EB-*m*-$Fe^{3+/2+}$ demonstrated n-type behavior with voltage

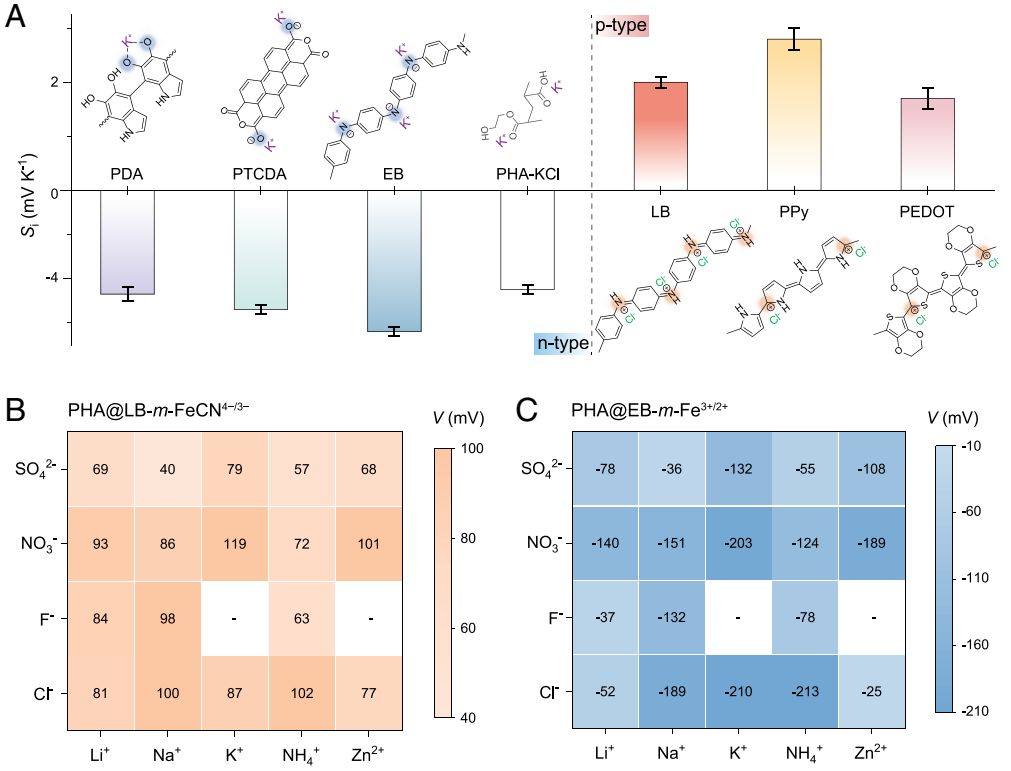

Fig. 5. Universality of the electrolyte doping strategy for ion control. (*A*) General demonstration of ion control in iTECs achieved by PHA-KCl-based hydrogels incorporating various p-type (LB, PPy, and PEDOT) and n-type (EB, PTCDA, and PDA) additives (Error bars are the SD of voltage recorded). Thermally induced voltage for (*B*) p-type PHA@LB-*m*-FeCN$^{4-/3-}$ and (*C*) n-type PHA@EB-*m*-Fe$^{3+/2+}$ at a ΔT of ~15 K (*m* represents the electrolyte salt used, concentration: 0.8 mol L^{-1}).

output range from −25 mV to −213 mV (Fig. 5*C*) across all dissolvable salts.

Discussion

In summary, we establish a general strategy to dope electrolytes by using electroactive conducting polymers to immobilize one type of ion: polymers with n-type reactions immobilize cations, leaving the electrolyte an anion conductor; and polymers with p-type reactions immobilize anions, leaving the electrolyte a cation conductor. We demonstrate this transformative capability by achieving n-type and p-type iTEC hydrogels using different electroactive additives and various salts. This ability enables us to optimize materials properties and achieve high thermopower in n-/p-type ionic hydrogels, by effectively regulating the thermodiffusion of ions (Cl^-, K^+) and the thermogalvanic process of redox couples ($FeCN^{4-/3-}$, $Fe^{3+/2+}$), transforming their interaction from antagonistic to synergistic effect via electrochemical doping. Although demonstrated in the context of thermoelectrochemical energy conversion, we anticipate that the electrolyte doping strategy will have broader impacts in other areas such as batteries, supercapacitors, and electrochemical sensors.

Materials and Methods

Materials. Aniline (AN, ≥99.5%), hydrazine monohydrate ($N_2H_4{\cdot}H_2O$, 64 to 65%), acrylic acid (AA, 99.0%), 2-hydroxyethyl methacrylate (HEMA, 97%), *N,N,N′,N′*-tetramethyl-ethylenediamine (TEMED, 99.0%), iron (III) chloride hexahydrate ($FeCl_3{\cdot}6H_2O$, ≥98.0%), potassium hexacyanoferrate (II) trihydrate ($K_4[Fe(CN)_6]{\cdot}3H_2O$, 98.5 to 102.0%), pyrrolidine (Py, 99%), 3,4-ethylenedioxythiophene (EDOT, 97%), dopamine hydrochloride (≥98%), perylene-3,4,9,10-tetracarboxylic dianhydride (PTCDA, 97%) were purchased from Sigma-Aldrich. Ammonium persulfate (APS, 98%) and iron (II) chloride tetrahydrate ($FeCl_2{\cdot}4H_2O$, 98%) were provided by Alfa Aesar. Hydrochloric acid (HCl, 37%) was obtained from Honeywell. Ammonium hydroxide ($NH_3{\cdot}H_2O$, 28 to 30%) was purchased from Thermo Scientific. Ethylene glycol dimethacrylate (EDGMA, >97.0%) was purchased from TCI. Potassium chloride (KCl, ≥99.0%) and potassium ferricyanide (III) ($K_3Fe(CN)_6$, 98.0%) were obtained from Fisher BioReagents and Acros Organics, respectively. Graphite paper (thickness: ~0.2 mm) was purchased from Langfang Zhongying Asbestos Chemical Co., Ltd. Activated carbon (YP-80F, specific surface area: ~2,100 m^2 g^{-1}) was provided by Kuraray Co., Ltd. All the chemicals were used directly without any purification.

Synthesis of ES-PANi. ES-PANi was prepared by a typical oxidation polymerization route. 10 mmol (0.914 mL) of AN monomer was dispersed in 90 mL of 0.5 mol L^{-1} HCl aqueous solution with continuous stirring for 30 min in an ice bath (0 ~ 5 °C). 10 mmol (2.28 g) of APS as oxidant/initiator was then dissolved into 10 mL of 0.5 mol L^{-1} HCl aqueous solution, and this APS solution was added dropwise into AN solution. After polymerizing for 24 h at ~3 °C, the precipitate was filtered and washed several times using deionized water and ethanol until the pH value of filtrate reached ~7. Finally, the dark green ES-PANi powder can be obtained after overnight drying at 60 °C in an oven.

Synthesis of EB Additive. EB was prepared by ES-PANi with $NH_3{\cdot}H_2O$ treatment. Typically, 100 mg of ES-PANi was dispersed in 5 mL of $NH_3{\cdot}H_2O$ aqueous solution (28 to 30 wt%) and vigorously stirred at room temperature for 24 h. After bringing the pH value to ~7 and drying, the dark blue EB powder can be obtained.

Synthesis of LB Additive. LB was prepared by ES-PANi with $N_2H_4{\cdot}H_2O$ treatment. Typically, 100 mg of ES-PANi was dispersed in 5 mL of $N_2H_4{\cdot}H_2O$ aqueous solution (~65 wt%) and stirred vigorously at 50 °C for 24 h. After bringing the pH value to ~7 and drying, the light blue LB powder can be obtained.

Fabrication of Hydrogel-Based iTECs. Typically, the YP-80F and polyvinylidene-fluoride binder in a mass ratio of 9:1 were well dispersed in *N*-methyl-2-pyrrolidone to form a homogeneous slurry, which was further painted on the graphite paper. As-prepared YP-80F coated graphite paper was cut into identical thin-rectangular shape with a dimension of 25 × 2 mm^2, and both electrodes were fixed on a polyethylene terephthalate (PET) substrate with a distance of 10 mm between the hot side and the cold side. The hydrogels (*SI Appendix, Supplementary Methods*) were

then carefully transferred to the related electrodes. Finally, the hydrogel-based iTEC was further encapsulated using polypropylene (PP) tape.

Construction of Flexible iTEC Modules. First, the cylindrical n-/p-type hydrogels (diameter: ~6 mm) were polymerized at ~50 °C using a tubular mold. After immersing in $FeCN^{4-/3-}$ and $Fe^{3+/2+}$ containing electrolytes and cutting into segments with a height of ~3 mm, the corresponding n-/p-type units for module assembly can be obtained. To keep the structural stability of n-/p-units, as-formed iTEC arrays are fully encapsulated by polydimethylsiloxane (PDMS). It is worth mentioning that a polyurethane (PU, Hale&Hearty) tape is employed as flexible substrate for scalable carbon electrode coating and device packaging. After sandwiching the n-p unit array with carbon electrodes coated PU films, a flexible module with tailored n-p units can be fabricated.

Thermoelectrochemical Measurements. All of the open circuit voltage–time and current–voltage curves of hydrogel-based iTECs were measured using an electrochemical workstation (CHI 660E). Two commercial Peltier plates (length: 40 mm, width: 40 mm) were used to generate temperature difference. As shown in *SI Appendix*, Fig. S38, two thermocouples were attached on the hot side and cold side of iTECs to monitor the temperature change directly. Moreover, the corresponding temperature differences and relative humidity were automatically controlled by dual-channel digital temperature control module (TCM-X207) and humidity generator (HumiSys, InstrQuest Inc.). In addition, the cold side and hot side were set as working electrode and counter/reference electrode during the thermoelectrochemical measurements. The cyclic stability of iTECs were conducted on a quasi-continuous working mode under a constant temperature difference with/without loading resistance. First, the iTECs were thermally charged in open-circuit without loading resistance and electrically discharged with loading a resistance (50 kΩ) for 20 s. Then, the iTECs were thermally recharged back to the relatively high open-circuit voltage in 20 s (without loading resistance). CV curves of iTECs were recorded by a three-electrode setup, in which one PC@G electrode was used as the working electrode while the graphite paper served as the counter electrode, and the Ag/AgCl electrode was employed as reference electrode. The potential ranges of CV tests were set as −1 to 1.2 V and −0.2 to 1.0 V for PHA@LB-KCl-$FeCN^{4-/3-}$ and PHA@EB-KCl-$Fe^{3+/2+}$ hydrogel-based iTECs, respectively. EIS analysis of module was tested in a frequency range of 100 mHz ~1 MHz with an amplitude of 5 mV.

Data, Materials, and Software Availability. Study data are included in the article and/or *SI Appendix*.

ACKNOWLEDGMENTS. This work is supported by the Ministry of Education, Singapore, under the Academic Research Fund Tier 2 (MOE-T2EP50124-0007, G.W.H.), Tier 1 (FY2023, 23-1156-A0001, G.W.H.), and NUS research support (A-8003994-00-00, G.W.H.). We thank Dr. C. Xu for helping with in situ Raman characterization and Dr. G. Tian, Dr. Y. Zhou and Prof. X. Zhang for their help and suggestions.

1. M. Massetti *et al.*, Unconventional thermoelectric materials for energy harvesting and sensing applications. *Chem. Rev.* **121**, 12465–12547 (2021).
2. J. Euvrard *et al.*, Electrical doping in halide perovskites. *Nat. Rev. Mater.* **6**, 531–549 (2021).
3. W. Jin *et al.*, Photocatalytic doping of organic semiconductors. *Nature* **630**, 96–101 (2024).
4. K. Wen *et al.*, Ion-dipole interaction regulation enables high-performance single-ion polymer conductors for solid-state batteries. *Adv. Mater.* **34**, 2202143 (2022).
5. T. Li *et al.*, Cellulose ionic conductors with high differential thermal voltage for low-grade heat harvesting. *Nat. Mater.* **18**, 608–613 (2019).
6. P. Tang, P. Jing, W. Tan, Q. Dou, X. Yan, Ion-confined transport supercapacitors: The encounter with energy electronics. *Mater. Today* **74**, 187–202 (2024).
7. X. Qian, Z. Ma, Q. Huang, H. Jiang, R. Yang, Thermodynamics of ionic thermoelectrics for low-grade heat harvesting. *ACS Energy Lett.* **9**, 679–706 (2024).
8. Z. Li, Y. Xu, X. Zhang, Progresses and insights of thermoelectrochemical devices for low-grade heat harvesting: From mechanisms, materials to devices. *Energychem* **6**, 100136 (2024).
9. Q. Yang *et al.*, Flexible thermoelectrics based on ductile semiconductors. *Science* **377**, 854–858 (2022).
10. Q. Zhang, K. Deng, L. Wilkens, H. Reith, K. Nielsch, Micro-thermoelectric devices. *Nat. Electron.* **5**, 333–347 (2022).
11. X. Shi, S. Song, G. Gao, Z. Ren, Global band convergence design for high-performance thermoelectric power generation in Zintls. *Science* **384**, 757–762 (2024).
12. C.-G. Han *et al.*, Giant thermopower of ionic gelatin near room temperature. *Science* **368**, 1091–1098 (2020).
13. L. Yin *et al.*, Low-temperature sintering of Ag nanoparticles for high-performance thermoelectric module design. *Nat. Energy* **8**, 665–674 (2023).
14. S. Sun, M. Li, X. L. Shi, Z. G. Chen, Advances in ionic thermoelectrics: From materials to devices. *Adv. Energy Mater.* **13**, 2203692 (2023).
15. B. Yu *et al.*, Thermosensitive crystallization-boosted liquid thermocells for low-grade heat harvesting. *Science* **370**, 342–346 (2020).
16. X. Shi, J. He, Thermopower and harvesting heat. *Science* **371**, 343–344 (2021).
17. J. Duan *et al.*, Liquid-state thermocells: Opportunities and challenges for low-grade heat harvesting. *Joule* **5**, 768–779 (2021).
18. Y. Han, J. Zhang, R. Hu, D. Xu, High-thermopower polarized electrolytes enabled by methylcellulose for low-grade heat harvesting. *Sci. Adv.* **8**, eabl5318 (2022).
19. Y. Zhu *et al.*, Ultra-high performance of ionic thermoelectric-electrochemical gel cells for harvesting low grade heat. *Energy Environ. Sci.* **17**, 4104–4114 (2024).
20. S. Wang *et al.*, High-performance cryo-temperature ionic thermoelectric liquid cell developed through a eutectic solvent strategy. *Nat. Commun.* **15**, 1172 (2024).
21. X. Lu *et al.*, Robust, efficient, and recoverable thermocells with zwitterion-boosted hydrogel electrolytes for energy-autonomous and wearable sensing. *Angew. Chem. Int. Ed. Engl.* **63**, e202405357 (2024).
22. Y. Liu *et al.*, Recurrently gellable and thermochromic inorganic hydrogel thermogalvanic cells. *Sci. Adv.* **10**, eadp4533 (2024).
23. S. Kim *et al.*, Realizing a high-performance n-type thermogalvanic cell by tailoring the thermodynamic equilibrium. *Energy Environ. Sci.* **17**, 8102–8110 (2024).
24. J. Hu *et al.*, Double selective ionic gel with excellent thermopower and ultra-high energy density for low-quality thermal energy harvesting. *Energy Environ. Sci.* **17**, 1664–1676 (2024).
25. C.-G. Han *et al.*, Remarkable high-temperature ionic thermoelectric performance induced by graphene in gel thermocells. *Energy Environ. Sci.* **17**, 1559–1569 (2024).
26. Z. Li *et al.*, Enabling giant thermopower by heterostructure engineering of hydrated vanadium pentoxide for zinc ion thermal charging cells. *Nat. Commun.* **14**, 6816 (2023).
27. L. Liu *et al.*, Strong tough thermogalvanic hydrogel thermocell with extraordinarily high thermoelectric performance. *Adv. Mater.* **35**, e2300696 (2023).
28. Z. Lei, W. Gao, P. Wu, Double-network thermocells with extraordinary toughness and boosted power density for continuous heat harvesting. *Joule* **5**, 2211–2222 (2021).
29. L. Jin, G. W. Greene, D. R. MacFarlane, J. M. Pringle, Redox-active quasi-solid-state electrolytes for thermal energy harvesting. *ACS Energy Lett.* **1**, 654–658 (2016).
30. T. Ding *et al.*, All-soft and stretchable thermogalvanic gel fabric for antideformity body heat harvesting wearable. *Adv. Energy Mater.* **11**, 2102219 (2021).
31. H. Zhou, T. Yamada, N. Kimizuka, Supramolecular thermo-electrochemical cells: Enhanced thermoelectric performance by host-guest complexation and salt-induced crystallization. *J. Am. Chem. Soc.* **138**, 10502–10507 (2016).
32. L. Liang *et al.*, A flexible quasi-solid-state thermoelectrochemical cell with high stretchability as an energy-autonomous strain sensor. *Mater. Horiz.* **8**, 2750–2760 (2021).
33. D. Zhang *et al.*, Stretchable thermogalvanic hydrogel thermocell with record-high specific output power density enabled by ion-induced crystallization. *Energy Environ. Sci.* **15**, 2974–2982 (2022).
34. Y. Wang *et al.*, In situ photocatalytically enhanced thermogalvanic cells for electricity and hydrogen production. *Science* **381**, 291–296 (2023).
35. Z. Guo *et al.*, Toward full utilization and stable cycling of polyaniline cathode for nonaqueous rechargeable batteries. *Adv. Energy Mater.* **13**, 2301520 (2023).
36. T. Shi *et al.*, Low-redox-barrier two-electron p-type phenoselenazine cathode for superior zinc-organic batteries. *Angew. Chem. Int. Ed. Engl.* **64**, e202501278 (2025).
37. N. Shpigel *et al.*, In situ real-time mechanical and morphological characterization of electrodes for electrochemical energy storage and conversion by electrochemical quartz crystal microbalance with dissipation monitoring. *Acc. Chem. Res.* **51**, 69–79 (2018).
38. N. Shpigel, M. D. Levi, D. Aurbach, EQCM-D technique for complex mechanical characterization of energy storage electrodes: Background and practical guide. *Energy Storage Mater.* **21**, 399–413 (2019).
39. M. D. Levi *et al.*, In situ electrochemical quartz crystal admittance methodology for tracking compositional and mechanical changes in porous carbon electrodes. *J. Phys. Chem. C* **117**, 14876–14889 (2013).
40. N. Shpigel *et al.*, Can anions be inserted into MXene? *J. Am. Chem. Soc.* **143**, 12552–12559 (2021).
41. J. Tang *et al.*, Infrared spectra of soluble polyaniline. *Synth. Met.* **24**, 231–238 (1988).
42. H. Lv *et al.*, Cross-linked polyaniline for production of long lifespan aqueous iron, organic batteries with electrochromic properties. *Nat. Commun.* **14**, 3117 (2023).
43. L. Yan *et al.*, Chemically self-charging aqueous zinc-organic battery. *J. Am. Chem. Soc.* **143**, 15369–15377 (2021).
44. M. E. Yvenat *et al.*, Study of the influence of the formation protocol on the SEI layer formed at the graphite electrode surface of a non-aqueous potassium-ion hybrid supercapacitor (KIC) through STEM and XPS analyses. *Sustain. Energ. Fuels* **7**, 4150–4159 (2023).
45. I. Noda, Generalized two-dimensional correlation method applicable to infrared, raman, and other types of spectroscopy. *Appl. Spectrosc.* **47**, 1329–1336 (1993).
46. Y. Gogotsi, R. M. Penner, Energy storage in nanomaterials-capacitive, pseudocapacitive, or battery-like? *ACS Nano* **12**, 2081–2083 (2018).
47. W. Gao, Z. Lei, W. Chen, Y. Chen, Hierarchically anisotropic networks to decouple mechanical and ionic properties for high-performance quasi-solid thermocells. *ACS Nano* **16**, 8347–8357 (2022).
48. Y. Li *et al.*, 3D hierarchical electrodes boosting ultrahigh power output for Gelatin-KCl-$FeCN^{4-/3-}$ ionic thermoelectric cells. *Adv. Energy Mater.* **12**, 2103666 (2022).
49. C. Xu, Y. Sun, J. Zhang, W. Xu, H. Tian, Adaptable and wearable thermocell based on stretchable hydrogel for body heat harvesting. *Adv. Energy Mater.* **12**, 2201542 (2022).
50. Y. Zong *et al.*, Bacterial cellulose-based hydrogel thermocells for low-grade heat harvesting. *Chem. Eng. J.* **433**, 134550 (2022).
51. J. Duan *et al.*, P-N conversion in thermogalvanic cells induced by thermo-sensitive nanogels for body heat harvesting. *Nano Energy* **57**, 473–479 (2019).
52. Y. Li *et al.*, Realizing record-high output power in flexible gelatin/GTA-KCl-$FeCN^{4-/3-}$ ionic thermoelectric cells enable by enlarging working temperature range. *Energy Environ. Sci.* **15**, 5379–5390 (2022).
53. Y. Zhang, P. S. Cremer, Interactions between macromolecules and ions: The Hofmeister series. *Curr. Opin. Chem. Biol.* **10**, 658–663 (2006).